Computer Methods in Biomechanics and Biomedical Engineering
iFirst article, 2011, 1–11

Taylor & Francis
Taylor & Francis Group

Numerical modelling of nanoparticle deposition in the nasal cavity and the tracheobronchial airway

Kiao Inthavong, Kai Zhang and Jiyuan Tu*

School of Aerospace, Mechanical and Manufacturing Engineering, RMIT University, PO Box 71, Bundoora, Vic 3083, Australia

(*Received 14 July 2009; final version received 12 May 2010*)

Recent advances in nanotechnology have seen the manufacture of engineered nanoparticles for many commercial and medical applications such as targeted drug delivery and gene therapy. Transport of nanoparticles is mainly attributed to the Brownian force which increases as the nanoparticle decreases to 1 nm. This paper first verifies a Lagrangian Brownian model found in the commercial computational fluid dynamics software Fluent before applying the model to the nasal cavity and the tracheobronchial (TB) airway tree with a focus on drug delivery. The average radial dispersion of the nanoparticles was 9x greater for the user-defined function model over the Fluent in-built model. Deposition in the nasal cavity was high for very small nanoparticles. The particle diameter range in which the deposition drops from 80 to 18% is between 1 and 10 nm. From 10 to 150 nm, however, there is only a small change in the deposition curve from 18 to 15%. A similar deposition curve profile was found for the TB airway.

Keywords: nanoparticle; nasal cavity; airway; deposition; CFD

Introduction

Exposure to airborne nanoparticles (nanoparticles; <100 nm) occurs from natural (forest fires, volcano lava, viruses) and unintentional sources (internal combustion engines, power plants, incinerators). More recently, advances in nanotechnology have seen the manufacture of engineered nanoparticles for many commercial and medical applications. Its importance in society is evident in the worldwide government investment that has increased by a factor of five from $825 million in 2000 to $4.1 billion in 2005 (Roco 2005). Engineered nanoparticles can exhibit large surface area to size ratio leading to greater biological activity. This increased biological activity can be desirable. For example, magnetic nanoparticles can be used for magnetic resonance imaging, targeted drug and gene delivery, tissue engineering, cell tracking and bioseparation (Gupta and Gupta 2005; McCarthy et al. 2007). However, the increased biological activity can also have adverse repercussions due to toxicity, induction of oxidative stress or of cellular dysfunction (Oberdörster et al. 2005).

During normal respiration, airborne particles are introduced into the respiratory system through nose or mouth inhalation, eventually depositing onto the respiratory organ walls, or finding its way to the lung airways. Toxicological risk assessment and/or pharmacological efficacy of nanoparticle delivery can be determined through the absorption of the nanoparticle upon deposition onto a surface. Transport of nanoparticles is mainly attributed to the Brownian diffusion which increases as the nanoparticle size decreases from 100 to 1 nm. The diffusion is caused by the Brownian force which is applied as an additional force acting on the body of the nanoparticle. It is normally reconstructed from the diffusion coefficient D via the Einstein relation $F = kTU/D$, where U is the particle velocity, T is the temperature of the medium and k is the Boltzmann constant.

Computational simulations have been performed to investigate the deposition sites of nanoparticles using two computational fluid dynamics (CFD) techniques. Firstly, the Eulerian approach performed by Yu et al. (1998) used CFX-F3D to simulate nanoparticles (1–10 nm) under a laminar constant flow rate of 15 l/min for the entire upper airway; Shi et al. (2006) used CFX 5.7 to study the transport and deposition of nanoparticles, under a transient laminar airflow for the nasal cavity; and Zhang et al. (2005) used CFX 4.4 to simulate nanoparticles for flow rates of 15–60 l/min for an idealised lung airway. In these studies, the Eulerian multi-component mixture approach was used to model the particle transport. The continuous fluid phase and the dilute particle phase are treated as interpenetrating fields, where Brownian motion is driven by a concentration gradient and a diffusion coefficient dependent on each individual particle size. This approach does not consider the particle inertia but provides simpler simulations and is efficient for a large number of particles. Secondly, the Lagrangian approach considers individual particle motion based on a force balance involving a variety of forces such as inertia, lift, thermophoretic and Brownian motion. A number of studies using the

*Corresponding author. Email: jiyuan.tu@rmit.edu.au

ISSN 1025-5842 print/ISSN 1476-8259 online

DOI: 10.1080/10255842.2010.493510
http://www.informaworld.com

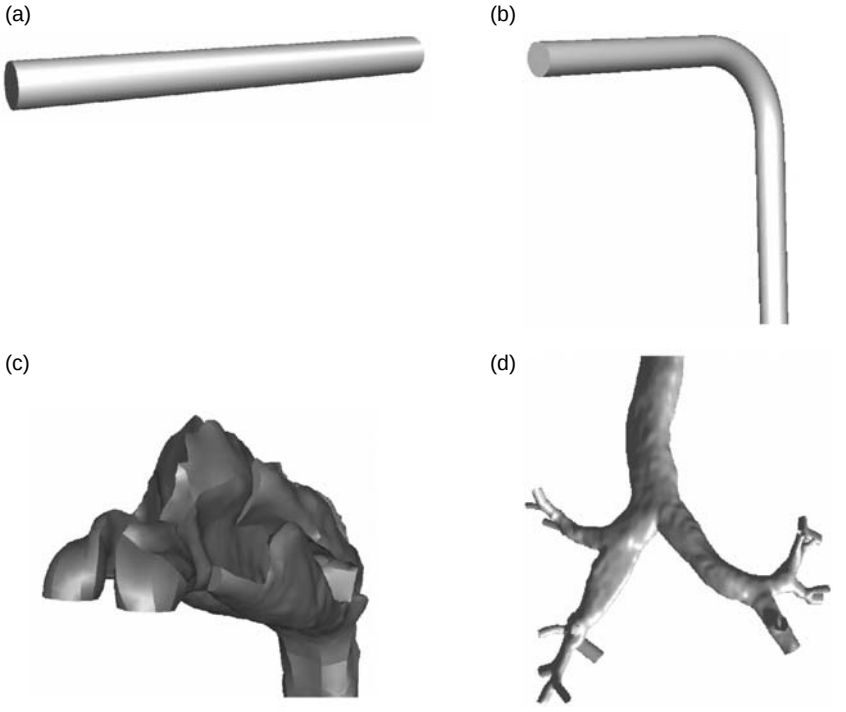

Figure 1. Reconstructed geometries of (a) straight pipe, (b) 90° bend pipe, (c) human nasal cavity and (d) human upper lung airway.

Lagrangian approach have been performed (Hofmann et al. 2003; Zamankhan et al. 2006; Longest and Xi 2007b). The work by Zamankhan et al. (2006) simulated submicron particles in the range of 1–100 nm under constant laminar flow rates between 4 and 14 l/min using the commercial CFD software Fluent. Brownian motion was accounted for through Fluent Brownian Model (Fluent-BM) derived from Li and Ahmadi (1992). The results corresponded well with experimental data. The results showed that the deposition efficiency was a function of $Q^a D_{\text{diff}}^b$, where Q (l/min) is the flow rate and D_{diff} (cm^2/s) is the particle diffusion coefficient. Also using Fluent, Longest and Xi (2007b) found that the Fluent-BM for 5–100 nm under-predicted diffusional deposition by up to one order of magnitude for flow rates of 15, 30 and 60 l/min. The differences in the results between the above two studies may be due to the rapid upgrades in the Fluent software in recent times, which have contributed to the detrimental implementation of the Fluent-BM.

This paper presents computational modelling techniques to track nanoparticles through the inhalation route within the nasal cavity and a six-generation tracheobronchial (TB) airway tree. Two realistic models developed from CT scans are used for the nasal cavity and the TB airway. The particles are tracked in the Lagrangian reference where the BM to be verified is matched against results from an Eulerian scheme and experimental data. The deposition efficiency and regional deposition patterns found will assist in dosimetric studies for efficient drug delivery, although it can also be applied to toxicology studies to evaluate the health effects of exposure to manufactured nanoparticles.

Method

Development of computational models

Four geometries are created for this study (Figure 1). The first two are a straight pipe and a 90°-bend pipe based on the analytic and experimental deposition data. The pipe models are used to validate the BM before finding the deposition data for the upper airway regions. For the human airways, CT scans provide the three-dimensional outline through the use of X-rays. However, this leads to radiation exposure of the patient. In order to reduce excessive radiation exposure, separate scans were taken of the nasal cavity and the lung airways from two different patients. Helical CT scans were used as the amount of time that the patient needs to lie down is reduced and therefore higher scan resolution can be achieved. A scan of the nasal cavity was obtained from a healthy 25-year-old Asian male (height 170 cm, weight 75 kg). The CT scan was performed using a CTI Whole Body Scanner (General Electric, USA). In a separate scan, images were obtained from a 66-year-old, non-smoking, asthmatic Asian male (height 171 cm and weight 58 kg) using a helical 64 slice multidetector row CT scanner (General Electric). Both scans acquired were of contiguous images (slices) of 1–5 mm thickness with voxel size of 0.625 × 0.625 × 1 mm. The field of view

was 40 cm, with a power of 120 kV peak and 200 mA. The CFD model was created using Mimics and GAMBIT software. Additional details can be found in Inthavong et al. (2009) and Inthavong, Wang, et al. (2008) for nasal cavity and lung airway construction, respectively. Table 1 summarises the geometries and some key dimensions.

Fluid flow modelling

The geometries were entered into a commercial CFD code, FLUENT 6.3.26, where the governing equations for fluid flow under steady-state conditions were modelled. Flow rates of 1, 10 and 60 l/min were used for the straight pipe and 90° bend pipe whereas a flow rate of 10 l/min was used for the nasal cavity and the lung airway. At 10 l/min, the flow regime in the respiratory airways has been determined as dominantly laminar (Hahn et al. 1993; Swift and Proctor 1977; Kelly et al. 2000; Zamankhan et al. 2006) and the quasi-steady assumption can be applied through the Womersley parameter and the Strouhal number (Wen et al. 2008). The steady-state continuity and momentum equations for the gas phase (air) in Cartesian tensor notation can be cast as

$$\frac{\partial}{\partial x_i}\left(\rho_g u_i^g\right) = 0, \tag{1}$$

$$u_j^g \frac{\partial u_i^g}{\partial x_j} = -\frac{1}{\rho}\frac{\partial p_g}{\partial x_i} + \frac{\partial}{\partial x_j}\left(\nu_g \frac{\partial u_i^g}{\partial x_j}\right), \tag{2}$$

where u_i^g is the ith component of the time-averaged velocity vector and ρ_g is the air density. The equations were discretised with the QUICK scheme whereas the pressure–velocity coupling was resolved through the SIMPLE method.

Particle flow modelling

For a low volume fraction of dispersed phase (particles), the Lagrangian approach with one-way coupling is used, i.e. the airflow transports the particles, but the effect of particle movements on the flow is neglected. In this approach, the airflow field is first simulated, and then the trajectories of individual particles are tracked by integrating a force balance equation on the particle, which can be written as

$$\frac{\mathrm{d}u_i^p}{\mathrm{d}t} = F_\mathrm{D} + F_\mathrm{g} + F_\mathrm{B} + F_\mathrm{L} + F_\mathrm{T}, \tag{3}$$

where F_g is the gravity term, which is defined as

$$F_\mathrm{g} = \frac{g(\rho_\mathrm{p} - \rho_\mathrm{g})}{\rho_\mathrm{p}}, \tag{4}$$

where ρ_p and ρ_g denote the density of particle material and air, respectively. F_D is the drag force per unit particle mass taking the form of Stokes' drag law (Ounis et al. 1991) defined as

$$F_\mathrm{D} = \frac{18\mu}{d_\mathrm{p}^2 \rho_\mathrm{p} C_\mathrm{c}}\left(u_i^g - u_i^p\right), \tag{5}$$

where C_c is the Cunningham correction factor to Stokes' drag law, which can be calculated from

$$C_\mathrm{c} = 1 + \frac{2\lambda}{d_\mathrm{p}}\left(1.257 + 0.4\,\mathrm{e}^{-\left(1.1 d_\mathrm{p}/2\lambda\right)}\right), \tag{6}$$

where λ is the mean free path of air, assumed to be 65 nm. Amplitudes of the Brownian force components are of the form

$$F_\mathrm{B} = \zeta\sqrt{\frac{\pi S_0}{\Delta t}}, \tag{7}$$

where ζ is a zero-mean, unit-variance independent Gaussian random number, Δt is the time-step for particle integration and S_0 is a spectral intensity function defined as

$$S_0 = \frac{216\nu k_\mathrm{B} T}{\pi^2 \rho d_\mathrm{p}^5 \left(\frac{\rho_\mathrm{p}}{\rho}\right)^2 C_\mathrm{c}}, \tag{8}$$

which is directly related to the diffusion coefficient. The Brownian force expression in Equation (7) can be

Table 1. Dimensions and details of the four geometries considered in this study.

	Inlet hydraulic diameter (D_h, cm)	Radius of curvature (cm)	Inlet flow rate (l/min)	Inlet Re number	Mesh size
Straight pipe	0.45	–	1	322	750,000
			15	4840	
			60	19,370	
90° bend pipe	0.46	1.43	1.052	305	550,000
Nasal cavity	1.0	1.50[a]	10	1452	1.4 million
6-Generation upper lung airway	1.8	–	10	807	1.3 million

[a] Nostril-nasal valve bend.

rearranged to highlight the diffusion coefficient as

$$F_{\mathrm{B}} = \frac{\zeta}{m_d}\sqrt{\frac{1}{\tilde{D}}\frac{2k_{\mathrm{B}}^2 T^2}{\Delta t}}, \tag{9}$$

where m_d is the mass of the particle, T is the absolute temperature of the fluid, ν is the kinematic viscosity, k_{B} is the Boltzmann constant and $\tilde{D}$ is the diffusion coefficient defined as

$$\tilde{D} = \frac{k_{\mathrm{B}} T C_{\mathrm{c}}}{3\pi\mu d_{\mathrm{p}}}. \tag{10}$$

The default Fluent-BM is turned off and in its place the equivalent theoretical force is re-entered as an additional body force. Thus, Equation (9) is entered into the user-defined function (UDF) option in Fluent and is referred to as (UDF-BM). The UDF-BM represents an alternative to the default method in which Fluent computationally processes the Brownian force applied to the particle. Saffman's lift force, or lift due to shear (Li and Ahmadi 1992), is a generalisation of the expression originally provided by Saffman (1965) and is applied here as

$$F_{\mathrm{L}} = \frac{2K\nu^{1/2}\rho d_{ij}}{\rho_{\mathrm{p}} d_{\mathrm{p}} (d_{lk} d_{kl})^{1/4}} \left(\vec{v} - \vec{v}_{\mathrm{p}}\right), \tag{11}$$

where K is a constant and is equal to 2.594, whereas d_{ij} is the deformation tensor. This form of lift force is intended for small-particle Reynolds numbers. Also, the particle Reynolds number based on the slip velocity must be smaller than the square root of the particle Reynolds number based on the shear field.

Small particles suspended in a gas that exhibits a temperature gradient experience a thermophoretic force in the direction opposite to that of the gradient. This effect is included in the thermophoretic force term,

$$F_{\mathrm{T}} = -D_{\mathrm{T}} \frac{1}{m_{\mathrm{p}} T} \frac{\partial T}{\partial i}, \tag{12}$$

where D_{T} is the thermophoretic coefficient given in Talbot et al. (1980). A particle rebounding from the surfaces was ignored and particle deposition was determined when the distance between the particle centre and a surface was less than or equal to the particle radius. The particle tracking is then terminated. For larger particles, the effects of particle contact may be considered if the particle is significantly solid. For nanoparticles especially in drug delivery in the respiratory airway, the drug solution may be aqueous and upon particle contact may be immediately absorbed by the respiratory walls. In this study, it was prudent to isolate the effects of the Brownian diffusion modelling from additional models in order to see the effects from BMs alone. For solid particles, the particle contact need to be considered, wall roughness and particle rebounding through the restitution coefficient needs to be applied as discussed in Tian et al. (2008). The deposition of particles will still be dominated by the random motion of Brownian diffusion when the particles are away from the wall. However, the particles may remain close to the wall due to the viscous effects within the boundary layer. The Eulerian approach to modelling the nanoparticle diffusion involves a single mixture fluid, with the nanoparticles treated as chemical species. A scalar c, representing the concentration of the nanoparticles, is applied to the transport equation

$$\frac{\partial\left(u_j c\right)}{\partial x_j} = \frac{\partial}{\partial x_j}\left[\left(\tilde{D} + \frac{\upsilon_{\mathrm{T}}}{S}\right)\frac{\partial c}{\partial x_j}\right], \tag{13}$$

which neglects the effects of particle inertia. Longest and Xi (2007a) showed that the effects of particle inertia play a minor role in ultrafine aerosol deposition and that inertia effects could be neglected for particle Stokes numbers below 5×10^{-5}.

Boundary conditions

In order to achieve a fully developed flow throughout the computational domain for the straight and 90° bend pipes, an additional separate pipe 5D in length with the same cross section and mesh was simulated with periodic boundaries. When the flow reached a fully developed state, the velocity profile of one cross section of the separate periodic straight pipe model was used as the inflow condition at the inlet of the 90° bend pipe and the straight pipe. Three flow rates were considered for the straight pipe, 1, 10 and 60 l/min, which reflect a very laminar flow, light breathing (turbulent) and heavy breathing (very turbulent), respectively. Inhalation through the nasal cavity is induced through the pressure difference caused by the movement of the diaphragm compressing and decompressing the lung. Therefore, the outlet of the nasal cavity (pharynx) was set as a negative pressure equivalent to a flow rate of 10 l/min relative to the atmospheric pressure set at the nostril inlets. This method presents a more realistic approach to nasal cavity modelling which was traditionally modelled with a uniform or developed velocity inlet at the nostrils (Keyhani et al. 1995; Inthavong et al. 2006).

Boundary conditions for the particles were set up as a circular particle release entrained in the flow field. Particles were released from 0.01 m from the inlet to prevent any spurious data exiting the inlet upon immediate release. In addition, the radial distance at which a particle was located was not less than 0.1 mm away from the wall to eliminate artificial immediate deposition on the walls. Turbulent dispersion is not considered in this study to isolate the effects of the Brownian motion at the higher

flow rate and instead the so-called mean-flow particle-tracking approach is used. In the Lagrangian tracking scheme, u_i^g found in the slip velocity $(u_i^g - u_i^p)$ in Equation (6) is defined from the cell centre and a particle within any part of that cell takes u_i^g from the cell centre. For cells adjacent to the wall boundaries, the velocity profile should approach zero at the wall rather than be uniform throughout the cell. Therefore, a near wall interpolation (NWI) scheme defined by

$$U_i^g = \frac{(U_1/L_1) + (U_2/L_2) + (U_3/L_3) + (U_4/L_4)}{(1/L_1) + (1/L_2) + (1/L_3) + (1/L_4)} \quad (14)$$

is applied to all wall-adjacent cells and is shown in Figure 2. The NWI takes into account the influence of the zero velocity at the wall boundary as well as the convective fluxes of the surrounding cells.

Preliminary analysis

To ensure statistical independence, mesh convergence as well as particle number independence tests was performed. The number of cells outlined in Table 1 reflects geometries that showed less than 1% change in velocity profiles when the mesh was further refined. The number of particles tracked was checked for statistical independence because the BM is inherently of a stochastic nature. This was determined by repeated simulations where the number of particles was increased until the deposition efficiency becomes independent of the number of particles. Independence was achieved for 70,000 particles, because an increase of particles to 100,000 particles yielded a difference of less than 1% in the deposition efficiency. The force term describing random Brownian motion, Equation (9), contains the time-step used for particle integration. As a result, the Brownian force is influenced by the size of the time-step selected. Preliminary testing confirmed the results of Longest and Xi (2007b) which showed that one integration step per control volume for the Fluent-BM and 10 integration steps for UDF-BM were the most suitable time-step sizes.

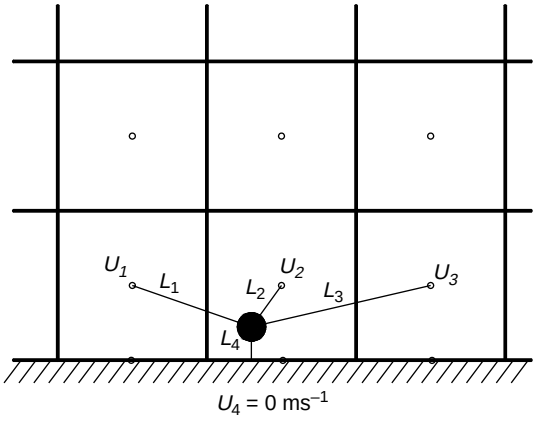

Figure 2. Near-wall interpolation scheme applied to all wall-adjacent cells.

Results and discussion

Deposition in fully developed pipes

Deposition results for the two Brownian motion models (Fluent-BM and the UDF-BM) are first verified through deposition efficiencies in the straight pipe and 90° bend pipe before applying the models to the nasal cavity and TB airway. The deposition efficiency from 1 to 100 nm simulated in a straight pipe and a 90° bend pipe us shown in Figure 3. The straight pipe was simulated under three different flow rates that are representative of a range of breathing levels found in the respiratory airways, whereas the bend pipe matched the flow conditions of Wang et al. (2002). For all cases, the Eulerian simulations capture well the particle diffusion. Some deviation from the empirical correlation of Ingham (1975) is found for particles approaching 100 nm. The correlation is given as

$$\mathrm{DE} = 1 - \left(0.819\,\mathrm{e}^{-14.63\Delta} + 0.0976\,\mathrm{e}^{-89.22\Delta} + 0.0325\,\mathrm{e}^{-228\Delta} + 0.0509\,\mathrm{e}^{-125.9\Delta^{2/3}}\right), \quad (15)$$

where

$$\Delta = \frac{DL_{\mathrm{pipe}}}{4U_{\mathrm{inlet}}R^2}. \quad (16)$$

Here, L_{pipe} is the pipe length, U_{inlet} is the inlet velocity and R is the pipe radius. In addition to the favourable results, the Eulerian model is also less computationally demanding because of the single convection–diffusion equation that governs the fluid–particle interaction (Equation (13)) when compared with the Lagrangian approach which requires a large number of particles to achieve a statistical average. In terms of computational efficiency, the Eulerian approach is by far superior. However, the Eulerian approach lacks the ability to resolve additional body forces that are applicable to each individual particle. In the Eulerian approach, the nanoparticles are treated as a dilute chemical species having a local mass fraction within a multi-component single fluid. The fluid transports the nanoparticle species under a convective flow, and the movement of the species from one computational cell to any adjacent cells is governed by the diffusion coefficient $\tilde{D}$ only. Thus, additional body forces such as inertia are not included. It has been shown by Longest and Xi (2007a) that particle inertia on area-averaged deposition efficiency needed to be considered for particle Stokes numbers above 5×10^{-5}. For the straight pipe, this corresponds only to

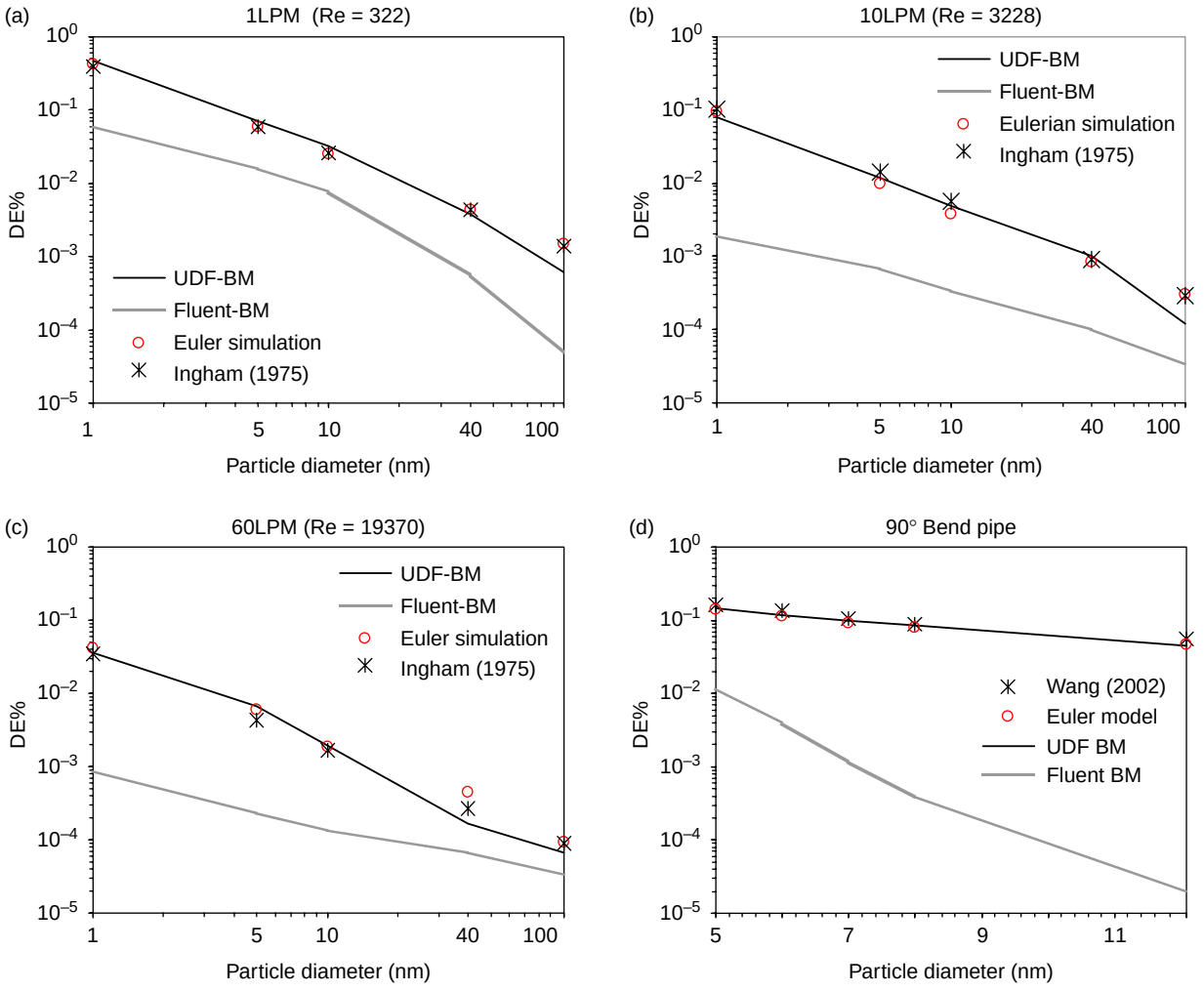

Figure 3. Deposition efficiency validation of the Fluent in-built BM and the UDF-BM model in (a) straight pipe 1LPM, (b) straight pipe 15LPM, (c) straight pipe 60LPM and (d) 90° bend pipe.

the larger particles under investigation, e.g. 40 and 100 nm particles at a flow rate of 60 l/min, and 100 nm at 15 l/min in the upper range of particles investigated. Furthermore, slip effects are not considered in the diffusion coefficient $\tilde{D}$, whereas it is included in the Lagrangian approach within the drag force through the Cunningham slip correction, C_c, applied onto the particles in Equations (5) and (6). The absence of the slip term becomes increasingly significant with decreasing particle size because C_c is an inverse exponential function of the particle diameter d_p. As discussed in Longest and Xi (2007b), the higher the slip, the weaker the coupling is between the particles and the fluid, leading to deviations from streamlines and increasing in the residence times. Therefore, the Lagrangian approach becomes important to resolve the inertial properties of particles, while also providing individual particle tracking in order to obtain highly detailed particle deposition patterns.

Verification of the numerical results from the Fluent-BM indeed confirms the fallibility of the Brownian motion when implemented through the default Fluent-BM. Large under-predictions are found for the Fluent-BM especially for 1-nm particles in the straight pipe, whereas for the bend pipe larger differences are found for 100 nm. The UDF-BM results on the other hand show improved results with the data matching the empirical correlation more closely. The Brownian diffusion process can be represented by a radial dispersion (or cloud dispersion) of the particle trajectory from its origin because the flow field is fully developed and therefore changes in the axial direction are non-existent. The average radial dispersion R_{ave} is simply the sum of the particles root-mean-square deviation or arc length from the origin divided by the number of particles sampled ($n = 70{,}000$).

$$R_{ave} = \frac{\sum_i^n \sqrt{x^2 + y^2}}{n_{particles}} \tag{17}$$

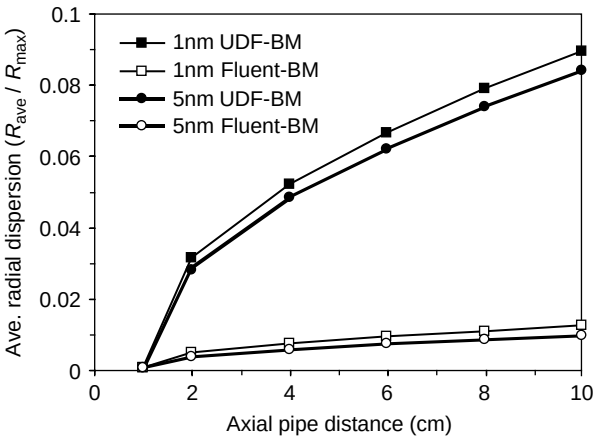

Figure 4. Cloud dispersion of 70,000 particles released from the radial centre of the straight pipe.

for the Fluent-BM and the UDF-BM is shown in Figure 4. The average dispersion of the 1-and 5-nm particles deviates as much as $0.09R$ (R = radius) distances from the origin. It must be noted that Figure 4 represents the average dispersion and that a proportion of particles will deviate much further than what the results displayed. In fact, for 1-nm particles, the UDF-BM found that 25% of particles released from the pipe centre deposited onto the walls. The Fluent-BM achieves very small radial dispersion, up to nine times less than the dispersion produced by the UDF-BM which leads to the large differences in the deposition efficiencies between the two models found in Figure 3. This suggests that the contribution of the Brownian force is not adequately achieved through the Fluent-BM whereas improved results are found for the UDF-BM.

One distinct advantage of using the Lagrangian approach for modelling nanoparticles is the ability to track the Brownian trajectory of individual particles. Visualisations of 1-nm particles released from the pipe centre at an axial distance of 1 cm downstream from the inlet are shown in Figure 5. The figure is a representative sample of 250 particles which shows the effects of the Brownian motion as the particles move through the pipe under a flow rate of 1 l/min. Adequate random fluctuations that are characteristic of Brownian motion are found in the UDF-BM where a proportion of the particles diffuse through the pipe far enough to deposit onto the edges of the walls. In contrast, the Fluent-BM produces insufficient Brownian force to allow the particles to diffuse further than $0.01R$ distances from the pipe centre. Consequently, the particles remain close to the pipe centre with the radial dispersion shown in Figure 5(d) being much smaller and narrower in comparison to that show in Figure 5(c),(d).

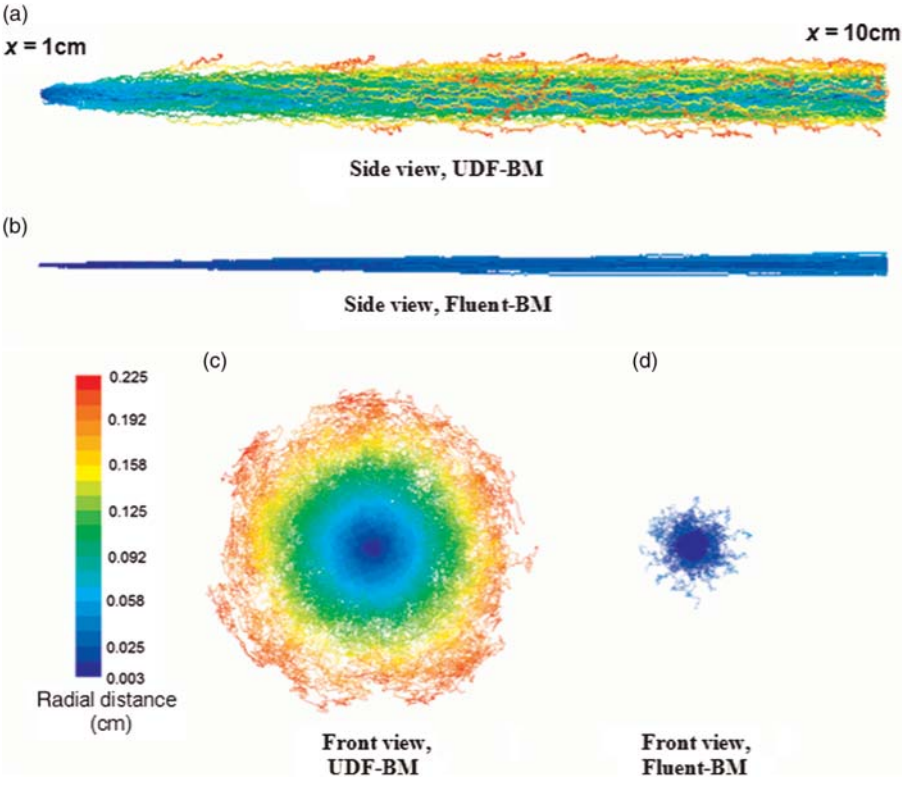

Figure 5. Trajectories of 1 nm particles released from the pipe centre superimposed onto the one image. Side view of trajectories in the straight pipe are shown in (a) and (b). Cross-sectional views from the outlet of the pipe looking upstream are shown in (c) and (d).

Deposition in a human nasal cavity

The published results for irregular geometries such as the oral cavity (Longest and Xi 2007b) found that it is necessary to include a NWI to adequately model local deposition of nanoparticles, whereas for regular geometries such as straight pipes and bend the deposition efficiency was found to be independent of the NWI, due to the ability to resolve the near-wall boundaries with high resolution. Comparisons of the simulated results were made with the available experimental data reported by Cheng et al. (1996) for different nasal cavities (Figure 6). Here, the solid line corresponds to the model prediction. The deposition curve is high for very small nanoparticles and the particle diameter range in which the deposition drops from 72 to 18% is between 1 and 10 nm. From 10 to 150 nm, however, there is only a small change in the deposition curve from 18 to 15%. This deposition curve profile is characteristic of the Brownian diffusion, where the particles are so small that the fluid may no longer be considered continuous. The trajectory of the nanoparticle is governed by a continuous (non-discrete) stochastic path caused by the kinetic impact of the air molecules under a thermally excited state (i.e. having a temperature) and concentration gradients. The diffusion coefficient which is the main contributor to the Brownian motion is proportional to the slip correction, C_c, and inversely proportional to particle size which explains the high gradient found in the deposition curve for particles in the range of 1–10 nm.

Local deposition patterns for a 1-nm particle are shown in Figure 7. A particle was deemed deposited if it impacted onto the wall surfaces, otherwise the particle escaped through the outlet. The deposition pattern is distributed evenly through the nasal cavity where the diffusion of 1-nm particles disperses the particles in all directions. The wall contours in Figure 7(c),(d) show the regional 'hot spots' of deposition which is determined by the number of particles that deposit onto a wall face divided the maximum number of particles that deposit on any one face. Few particles are able to reach the wider meatus region, and instead rather the particles remain close to the nasal septum wall (inner regions). The local hot spot is found at the upper regions of the cavity with a higher distribution of deposition within that one area.

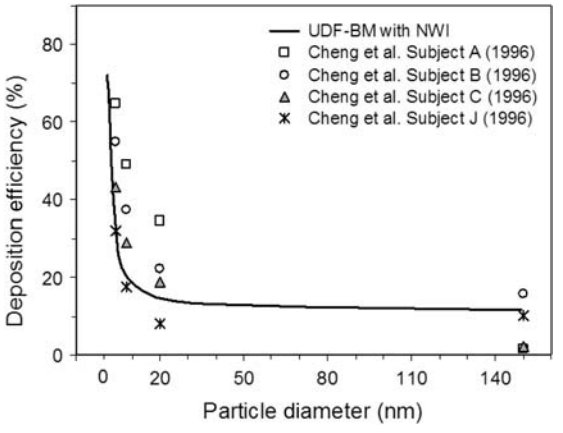

Figure 6. Deposition efficiency of 1–150-nm particles in a human nasal cavity at a steady inhalation rate of 10 l/min.

In general, the deposition pattern is spread out through the nasal cavity wall produce. This has interesting applications for drug delivery where traditional nasal sprays micron-sized droplets that are prone to inertial deposition. This deposition mechanism leads to high inertial impaction (up to 100% for the mean atomised particle droplet of 50 μm) in the anterior region of the nasal cavity (Inthavong et al. 2006; Inthavong, Tian, et al. 2008). However, for high drug efficacy, the drug droplets need to be deposited in the middle regions of the nasal cavity, where the highly vascularised walls exist. Smaller particles of 1 μm sizewere found to be less affected by inertial properties, which allowed it to bypass the anterior region of the nasal cavity. However, because of the particles ability to follow the streamlines more readily, the particles were less likely to deposit in any region of the nasal cavity and would bypass it completely, leading to the undesired effects of lung deposition. Delivery of nanoparticles especially 1–5-nm particles, therefore, can provide improved deposition in the middle regions while minimising deep lung deposition.

Deposition in a human upper lung airway

The contribution of the total deposition efficiency within the trachea, right cavity side and the left cavity side for a range of 1–50-nm particles is shown in Figure 8. The total deposition is defined as the number of particles depositing within a region divided by the total number of particles introduced into the computational domain. The largest proportion of deposition is found in the right-cavity side, nearly doubling the deposition in the left-cavity side, for this particular 6-generation TB airway. Maximum deposition is found for 1-nm particles as expected and the deposition curve drops rapidly before flattening out at approximately for 10-nm particles, similar to the deposition curve found for the nasal cavity. The lower deposition found in the trachea may be caused by the larger diameter and short length of the trachea relative to the small branch diameters and cumulative length of the daughter and sub-daughter bifurcating airway branches. The total deposition efficiency shows a larger number of particles depositing in the right-cavity side. However, this may be a consequence of the air flow field. Table 2 shows an analysis of the particle flow distribution and also the local deposition efficiency. From the particle flow distribution, it is evident that approximately two-thirds of the particles are flowing through the right cavity.

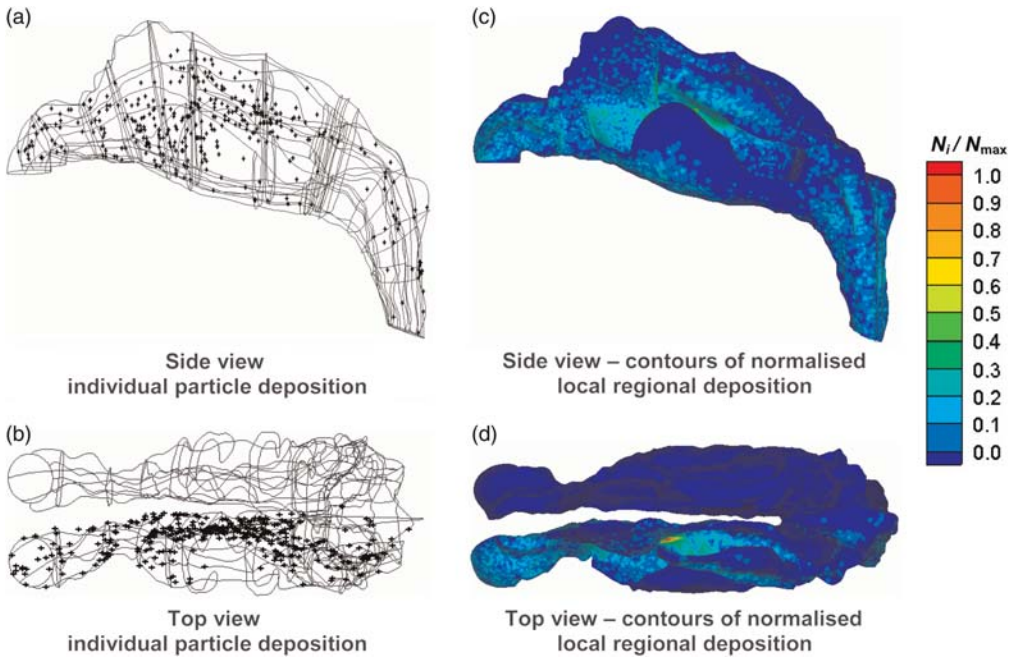

Figure 7. Regional deposition patterns of 1-nm particles under a flow rate of 10 l/min in a human nasal cavity.

Because the diffusion is a random process away from the convective streamlines, the flow distribution will also be approximately two-thirds. Flow patterns for the same TB airway have been published in Inthavong, Yong, et al. (2008) which demonstrate this flow distribution and the distribution from Smith et al. (2001) also concurs which found a flow distribution biased towards the right-cavity side with a ratio of 62:38. When considering the local deposition efficiency, which is defined as the number of particles depositing onto the wall of a region divided by the number of particles entering that same region, the deposition efficiency of the particles in either cavity side

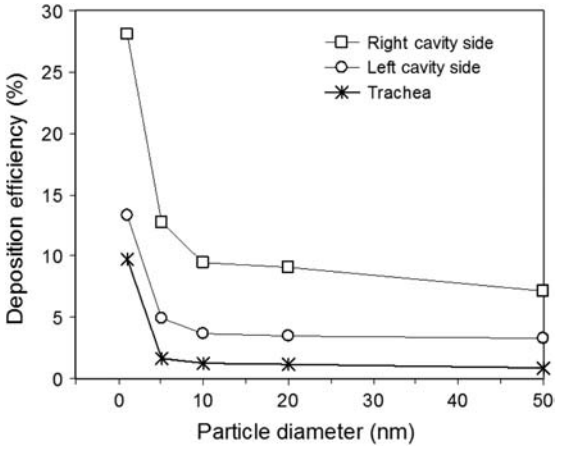

Figure 8. Deposition efficiency of 1–150 nm particles in a human upper lung airway at a steady inhalation rate of 10 l/min.

is actually similar. This is reasonable because the Brownian diffusion causes the particles to disperse randomly, and if the airway geometry does not exhibit large differences, then from a large sample of particles, the random dispersion should equate within each cavity side. The deposition patterns in Figure 9 show high concentration at the carinal ridges and the inside walls around the carinal ridges. This pattern is also confirmed by Zhang et al. (2005) which attributes the deposition to complicated air flows and large particle concentration gradients in these regions. The complicated air flows may be the flow bifurcation which exhibit sharp pressure gradients leading to localised recirculating regions. The large particle concentration gradient attribute is found by the high concentration just upstream of the carina and zero concentration at the carinal ridge. This local hot spot is found at each bifurcating branch. Contours of normalised local regional deposition show the higher deposition in the right airway side, which is influenced by the biased flow distribution.

The deposition of 1-nm particles is quite high, reaching 50% total deposition in the TB airway whereas for the nasal cavity it reaches 81%. This paper provides a comparative study of the application of a verified BM, and based on the deposition results and the inclusion of a more complete respiratory airway model (i.e. nose to larynx to TB airway), it is unlikely that any 1-nm particles could reach the TB airway. This reinforces the potential of 1 nm being used for nasal drug delivery where the risk of deep lung deposition is negated.

Table 2. Particle flow distribution, total and local deposition comparisons in the TB airway.

		Local deposition efficiency			Particle flow distribution	
Particle diameter	Total deposition (%)	Trachea (%)	Left (%)	Right (%)	Left (%)	Right (%)
1	51.1	9.7	45.0	46.3	32.8	67.2
5	19.4	1.7	17.3	18.3	29.2	70.8
10	14.4	1.2	11.6	14.2	32.2	67.8
20	13.8	1.2	11.1	13.6	32.3	67.7
50	11.3	0.9	12.4	11.2	29.4	70.6

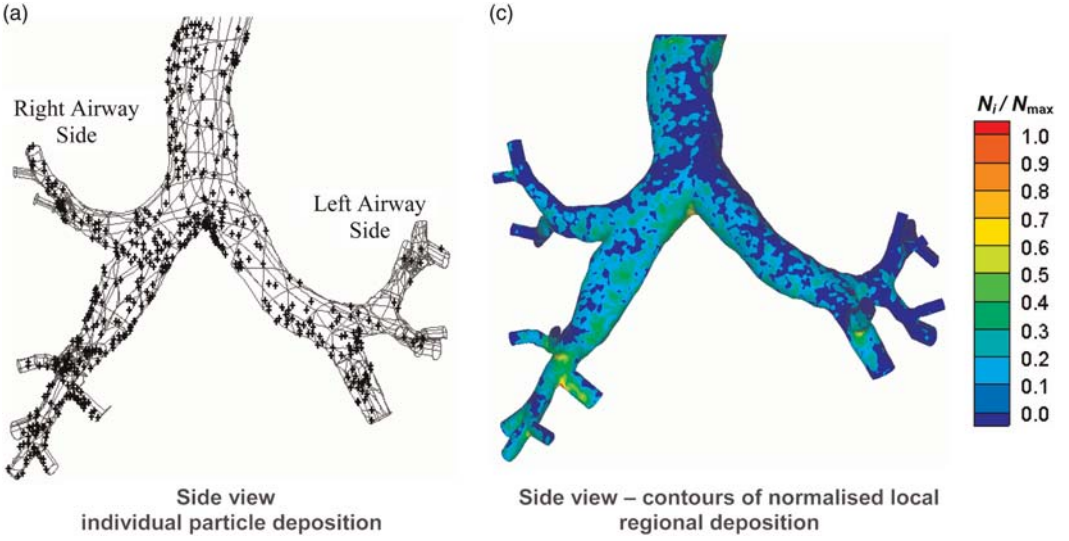

Figure 9. Regional deposition patterns of 1-nm particles under a flow rate of 10 l/min in a human upper lung airway.

Conclusion

Nanoparticles deposition in a human nasal cavity and the TB airway was simulated. To allow visualisation of individual particle deposition, the Lagrangian particle tracking scheme was used. However, using the commercial CFD software Fluent, it was confirmed in this paper that the Fluent-BM does indeed under-predict the diffusion deposition of ultrafine aerosols by up to one order of magnitude. When the Brownian force is entered as a custom UDF (UDF-BM), the results were improved. The average radial dispersion of 1-and 5-nm particles showed that the Fluent-BM produces much smaller dispersion from the pipe centre, up to nine times less than the dispersion produced by the UDF-BM. This implies that the contribution of the Brownian force on the total body forces on the particle is inadequately resolved from the Fluent-BM resulting in the convective influence to dominate.

Deposition of the nanoparticles in the nasal cavity and TB airway was high for very small nanoparticles (≈ 1 nm) and the particle diameter range in which the deposition drops from 72 to 18% is between 1 and 10 nm. From 10 to 150 nm, however, there is only a small change in the deposition curve from 18 to 15%. In general, the deposition pattern is spread out through the respiratory airways. The application of the deposition results and patterns on drug delivery was discussed where a potential opportunity exists to develop nanoparticles to increase deposition in the middle turbinate regions of the nasal cavity where the highly vascularised mucosal walls exist. Furthermore, the deposition of 1-nm particles reaching 81% in the nasal cavity means that the likelihood of 1-nm particles reaching the TB airway may be minimal given that the airway models in this study were separate from each other and the larynx was omitted. The results can be also interpreted for toxicological studies which see 1-nm particles being filtered within the nasal cavity; however, the adverse health effects of toxic nanoparticle absorption may be problematic.

Acknowledgements

The financial support provided by the Australian Research Council (project ID LP0989452) and by the RMIT University through an Emerging Research Grant is gratefully acknowledged.

References

Cheng KH, Cheng YS, Yeh HC, Guilmette A, Simpson SQ, Yang YH, Swift DL. 1996. *In-vivo* measurements of nasal airway dimensions and ultrafine aerosol deposition in the human nasal and oral airways. J Aerosol Sci. 27:785–801.

Gupta AK, Gupta M. 2005. Synthesis and surface engineering of iron oxide nanoparticles for biomedical applications. Biomaterials. 25:3995–4021.

Hahn I, Scherer PW, Mozell MM. 1993. Velocity profiles measured for airflow through a large-scale model of the human nasal cavity. J Appl Physiol. 75:2273–2287.

Hofmann W, Golser R, Balashazy I. 2003. Inspiratory deposition efficiency of ultrafine particles in a human airway bifurcation model. Aerosol Sci Technol. 37:988–994.

Ingham DB. 1975. Diffusion of aerosols from a stream flowing through a cylindrical tube. J Aerosol Sci. 6(2):125–132.

Inthavong K, Tian ZF, Li HF, Tu JY, Yang W, Xue CL, Li CG. 2006. A numerical study of spray particle deposition in a human nasal cavity. Aerosol Sci Technol. 40:1034–1045.

Inthavong K, Tian ZF, Tu JY, Yang W, Xue C. 2008. Optimising nasal spray parameters for efficient drug delivery using computational fluid dynamics. Comput Biol Med. 38: 713–726.

Inthavong K, Wang S, Wen J, Tu JY, Xue C. 2008. Comparison of micron and nano particle deposition patterns in a realistic human nasal cavity. 13th International Conference on Biomedical Engineering (ICBME2008), Singapore.

Inthavong K, Wen J, Tu JY, Tian ZF. 2009. From CT scans to CFD modelling – fluid and heat transfer in a realistic human nasal cavity. Eng Appl Comput Fluid Mech. 3:321–335.

Inthavong K, Yong Y, Ding S, Tu JY, Subic A, Thien F. 2008. Comparative study of the effects of acute asthma in relation to a recovered airway tree on airflow patterns. 13th International Conference on Biomedical Engineering (ICBME2008), Singapore.

Kelly JT, Prasad AK, Wexler AS. 2000. Detailed flow patterns in the nasal cavity. J Appl Physiol. 89:323–337.

Keyhani K, Scherer PW, Mozell MM. 1995. Numerical simulation of airflow in the human nasal cavity. J Biomech Eng. 117:429–441.

Li A, Ahmadi G. 1992. Dispersion and deposition of spherical particles from point sources in a turbulent channel flow. Aerosol Sci Technol. 16:209–226.

Longest PW, Xi J. 2007a. Computational investigation of particle inertia effects on submicron aerosol deposition in the respiratory tract. J Aerosol Sci. 38:111–130.

Longest PW, Xi J. 2007b. Effectiveness of direct Lagrangian tracking models for simulating nanoparticle deposition in the upper airways. Aerosol Sci Technol. 41:380–397.

McCarthy JR, Kelly KA, Sun EY, Weissleder R. 2007. Targeted delivery of multifunctional magnetic nanoparticles. Nanomedicine. 2:153–167.

Oberdörster G, Oberdörster E, Oberdörster J. 2005. Nanotoxicology: an emerging discipline evolving from studies of ultrafine particles environmental health perspectives. Environ Health Perspect. 113:823–839.

Ounis H, Ahmadi G, McLaughlin JB. 1991. Brownian diffusion of submicrometer particles in the viscous sublayer. J Colloid Interf Sci. 143:266–277.

Roco MC. 2005. International perspective on government nanotechnology funding in 2005. J Nanoparticle Res. 7(6): 707–712.

Saffman PG. 1965. The lift on a small sphere in a slow shear flow. J Fluid Mech. 22:385–400.

Shi H, Kleinstreuer C, Zhang Z. 2006. Laminar airflow and nanoparticle or vapor deposition in a human nasal cavity model. J Biomech Eng. 128:697–706.

Smith S, Cheng YS, Yeh HC. 2001. Deposition of ultrafine particles in human tracheobronchial airways of adults and children. Aerosol Sci Technol. 35:697–709.

Swift DL, Proctor DF. 1977. Access of air to the respiratory tract. In: Brain JD, Proctor DF, Reid LM, editors. Respiratory defence mechanisms. New York, NY: Marcel Dekker. p. 21–40.

Talbot L, Cheng RK, Schefer RW, Willis DR. 1980. Thermophoresis of particles in a heated boundary layer. J Fluid Mech. 101:737–758.

Tian ZF, Inthavong K, Tu JY, Yeoh GH. 2008. Numerical investigation into the effects of wall roughness on a gas-particle flow in a 90-degree bend. Int J Heat Mass Transfer. 51:1238–1250.

Wang J, Flagan RC, Seinfeld JH. 2002. Diffusional losses in particle sampling systems containing bends and elbows. J Aerosol Sci. 33:843–857.

Wen J, Inthavong K, Tu JY, Wang S. 2008. Numerical simulations for detailed airflow dynamics in a human nasal cavity. Respir Physiol Neurobiol. 161:125–135.

Yu G, Zhang Z, Lessman R. 1998. Fluid flow and particle deposition in the human upper respiratory system. Aerosol Sci Technol. 28:146–158.

Zamankhan P, Ahmadi G, Wang Z, Hopke PH, Cheng YS, Su WC, Leonard D. 2006. Airflow and deposition of nanoparticles in a human nasal cavity. Aerosol Sci Technol. 40:463–476.

Zhang Z, Kleinstreuer C, Donohue JF, Kim CS. 2005. Comparison of micro- and nano-size particle depositions in a human upper airway model. J Aerosol Sci. 36:211–233.